

Variable-Density Adaptive Imaging for High-Resolution Coronary Artery MRI

Marshall S. Sussman,^{1*} Jeffrey A. Stainsby,¹ Normand Robert,¹ Naeem Merchant,² and Graham A. Wright^{1,3}

Variable-density (VD) spiral *k*-space acquisitions are used to acquire high-resolution (0.78 mm), motion-compensated images of the coronary arteries. Unlike conventional methods, information for motion compensation is obtained directly from the coronary anatomy itself. Specifically, periods of minimal coronary distortion are identified by applying the correlation coefficient template matching algorithm to real-time images generated from the inner, high-density portions of the VD spirals. Combining the data associated with these images together, high-resolution, motion-compensated coronary images are generated. Because coronary motion is visualized directly, the need for cardiac-triggering, breath-holding, and navigator echoes is eliminated. The motion compensation capability of the technique is determined by the inner-spiral spatial and temporal resolution. Results indicate that the best performance is achieved using inner-spiral images with high spatial resolution (1.6–2.9 mm), even though temporal resolution (four to six independent frames per second) suffers as a result. Image quality within the template region in healthy volunteers was found to be comparable to that achieved with cardiac-triggered breath-hold scans, although extended acquisition times of around 5 min were needed to overcome reduced SNR efficiency. Magn Reson Med 48: 753–764, 2002. © 2002 Wiley-Liss, Inc.

Key words: variable-density; template matching; coronary artery; motion compensation; real-time

Diagnostic-quality MR coronary images must possess submillimeter spatial resolution. While the theoretical limits of MR do not preclude the attainment of such resolutions, respiratory- (1) and cardiac- (2) induced displacement and distortion (3) of the arteries can significantly degrade image quality. To counteract these effects, motion compensation schemes have been developed (4,5). With the evolution toward higher-resolution imaging, however, a number of concerns are arising with respect to their accuracy. Most of these approaches use indirect measures such as the position of bellows placed over the chest, ECG waveforms, and diaphragm position determined by navigator echoes to infer coronary motion. Recent studies have indicated that while indirect measures may correlate with

coronary displacement, they do not give a precise characterization of the actual motion (1,6,7). Additionally, indirect measures generally do not give any indication of the degree of distortion associated with the coronary motion (3). Furthermore, arrhythmias and/or difficulties in breath-holding, commonly found in patients with coronary disease, give rise to added difficulties in the application of these techniques (8).

A technique that makes use of direct visualization of the coronary anatomy for motion compensation was developed recently by Hardy et al. (9). In this “adaptive averaging” technique, a series of interleaved high-resolution echo-planar images are acquired. From each of the individual interleaves, aliased “subimages” are formed. Since these subimages are generated from every interleaf, they provide real-time visualization of the coronary anatomy. Each subimage is used to evaluate the motion present during the acquisition of the interleaf. If significant motion is detected, the interleaf is rejected. Since this motion compensation technique makes use of direct coronary visualization, the need for cardiac-triggering, navigator echoes, and breath-holding is eliminated. The major disadvantage with this approach is that the aliasing present in the subimages can obscure the anatomy of interest, and thus degrade the quality of the motion characterization. Furthermore, for a fixed readout time, the higher the resolution in the full echo-planar image, the greater the aliasing in the subimages.

In the present study, high-resolution images are generated through an adaptive imaging technique employing a series of variable-density (VD) spiral acquisitions (10). Motion and distortion information is provided directly from real-time lower-resolution images of the coronary anatomy generated from the inner, high-density portion of the VD spiral. The major advantage of this approach is that the inner-spiral images do not contain any aliasing. As a result, the displacement and distortion of the anatomy contained within these images can be evaluated precisely and quantitatively. Furthermore, the full VD spiral may be designed to achieve an arbitrary resolution, without any concomitant degradation in the quality of the inner-spiral images. In fact, a broad range of inner/outer spatial and temporal resolutions are made possible by varying the VD-spiral design.

In this study, VD adaptive imaging is used to acquire submillimeter resolution coronary artery images. Information for motion compensation is provided from the acquired VD data alone, with no additional cardiac-triggering, navigator echoes or breath-holding used. In the following sections, the image acquisition and prospective motion compensation strategy are described. The relationship between the inner-spiral spatial and temporal resolu-

¹Department of Medical Biophysics, Sunnybrook and Women's College Health Sciences Center, University of Toronto, Toronto, Canada.

²University Health Network, University of Toronto, Toronto, Canada.

³ASL-West, GE Medical Systems, Menlo Park, California.

Grant sponsor: Heart and Stroke Foundation of Canada; Grant sponsor: Canadian Institutes of Health Research.

*Correspondence to: Marshall S. Sussman, Rm. S612, Imaging Research Program, Sunnybrook and Women's College Health Sciences Center, University of Toronto, 2075 Bayview Ave., Toronto, Ontario M4N 3M5, Canada. E-mail: marshall@sten.sunnybrook.utoronto.ca.

Received 21 November 2001; revised 20 June 2002; accepted 2 July 2002.

2002 ISMRM Young Investigator I.I. Rabi Award Finalist.

DOI 10.1002/mrm.10275

Published online in Wiley InterScience (www.interscience.wiley.com).

© 2002 Wiley-Liss, Inc.

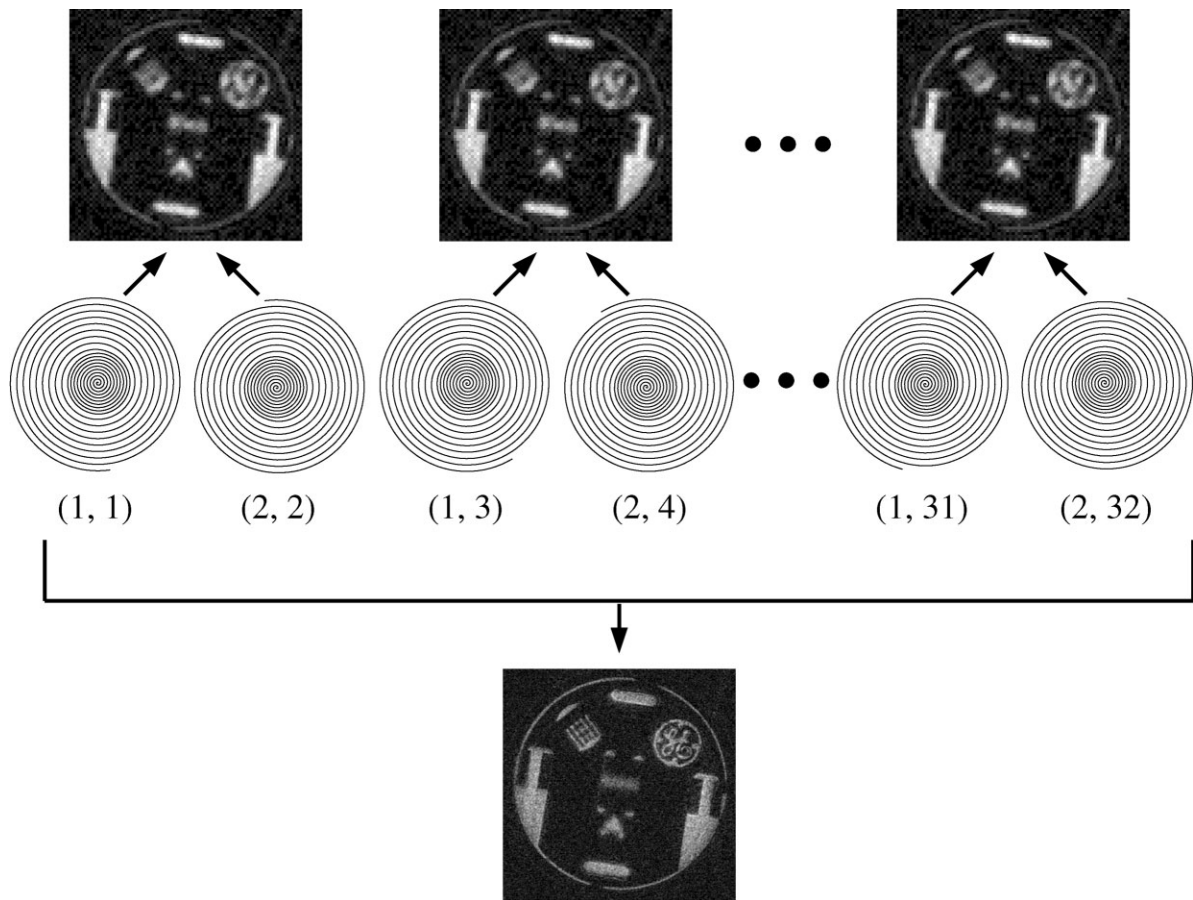


FIG. 1. VD acquisition of a phantom. In this example, the full VD spiral requires 32 interleaves ($=n_o$) for 0.75-mm resolution. However, low-resolution (3.5 mm), non-aliased images can be generated continuously throughout the scan from the inner-spiral data of every set of two interleaves ($=n_i$). The pair of numbers below each spiral corresponds to the inner and outer interleaf number, respectively. In general, n_o/n_i inner-spiral images can be formed from a complete VD-spiral acquisition.

tion, and motion compensation performance is explored. Results are compared with coronary images acquired with conventional cardiac-triggered breath-hold scans in healthy subjects.

THEORY

Motion Compensation With Variable-Density Spirals

The VD-spiral technique requires a time period spanning multiple cardiac and respiratory cycles to achieve high resolution. However, unlike other MR techniques, motion compensation information can be extracted directly and continuously from the data acquired for imaging the coronary artery itself. This is possible because VD spirals consist of two distinct components: a high-density inner spiral, and a low-density outer spiral (Fig. 1). The outer spiral is designed to form a high-resolution image after n_o interleaves. The inner spiral, while contributing to the high-resolution image, is designed to generate non-aliased, low-resolution images after every set of n_i interleaves, where $n_i < n_o$. If n_i is sufficiently small and the repetition time (TR) is short, these inner-spiral images can be acquired and reconstructed in real time. Consequently, while the total data acquisition time for the high-resolu-

tion image may be long, the coronary arteries can be visualized directly and continuously throughout the scan. From an analysis of the coronary anatomy contained within the inner-spiral images, data acquired during periods of minimal distortion can be identified. The associated full-spiral data can then be combined into a motion-compensated, high-resolution image.

Variable-Density Spiral Design

The motion compensation performance of the VD-spiral adaptive imaging technique is ultimately affected by the inner-spiral spatial and temporal resolution. In this study, the motion compensation performance of a range of inner-spiral spatial/temporal resolution combinations are explored. These combinations are affected by five interdependent parameters in the VD-spiral design: number of inner/outer spirals, readout time, fraction of readout time occupied by the inner spiral, and the field of view (FOV). To provide a fair comparison between different VD-spiral types, four design constraints were enforced:

1. The total readout time was maintained constant at 16 ms to minimize the effects of off-resonance blurring (11).

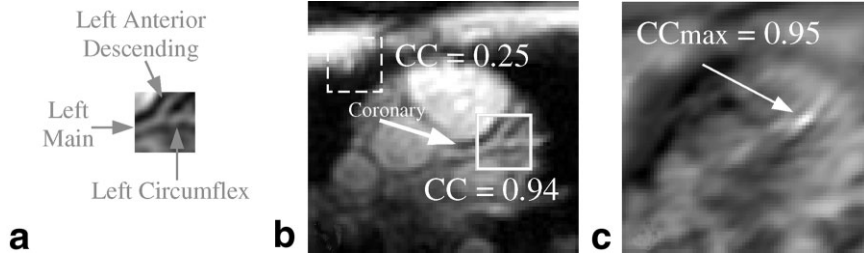


FIG. 2. The CC template matching technique. **a:** A template containing the left coronary artery is extracted from an initial real-time inner-spiral image. **b:** The CC values between the template and different locations in a subsequent inner-spiral image indicate the degree of similarity with the template at each location. The larger the CC value, the greater the similarity, up to a maximum of one for identity. In this case, the region close to the artery has a much higher CC value than the region near the chest wall. **c:** Image of the CC value at every location in the image. The location with the largest CC value ($=CC_{max}$) bears the greatest similarity to, and is the most probable position of, the template in the image.

2. The full-spiral resolution was kept constant at 0.78 mm.
3. The FOV, and hence the minimum required sampling density for inner- and full-spiral data sets, was kept constant at 20 cm.
4. The total scan time was kept (roughly) constant for all VD-spiral types. As per the algorithm described later, total scan time is proportional to the number of identical inner-spiral images that need to be identified ($=n_o/n_i$) and the number of averages ($\equiv NEX$):

$$\text{scan time} \propto (n_o/n_i) \cdot NEX. \quad [1]$$

The last constraint may result in different SNRs for different VD-spiral types, since:

$$\text{data acquisition time} = n_o \cdot NEX \cdot (\text{readout time}) \quad [2]$$

and SNR is proportional to $\sqrt{\text{data acquisition time}}$. In this study, a variety of VD spirals were designed to provide a reasonable range of inner-spiral spatial and temporal resolutions.

VD Adaptive Imaging Technique

In VD adaptive imaging, motion compensation is accomplished by prospectively minimizing the respiratory- and cardiac-induced distortion of the coronary anatomy in a region of interest (ROI). Initially, one of the inner-spiral real-time coronary images is chosen as a reference. A sub-region of the reference image containing the coronary artery of interest is saved as a template (Fig. 2a). Subsequent acquisition strategy is designed to minimize the amount of distortion in the acquired data relative to this initial template. An overview of the VD adaptive imaging technique is given in the flow chart of Fig. 3.

After template selection, n_i interleaves are acquired. The inner-spiral data from these interleaves are used to form a complete low-resolution image. However, along with the low-resolution information, n_i of the n_o outer spiral interleaves have also been acquired. As an example, in Fig. 1, the indices of the acquired inner, outer interleaves would be (inner, outer) = (1, 1) and (2, 2). After this initial step,

a second set of n_i interleaves is acquired. The inner-spiral interleaves from this set are identical to the previous ones, and can be used to form a new low-resolution image. The outer spiral interleaves, however, are different. With respect to Fig. 1, the newly acquired indices would be (1, 3) and (2, 4). Therefore, a total of $2 \cdot n_i$ unique outer interleaves, and two sets of the same n_i inner-interleaves have been acquired. This process continues until all n_o outer spiral interleaves have been acquired (stage A in Fig. 3). Note that in acquiring all n_o outer spiral interleaves, a total of n_o/n_i inner-spiral images will have been generated due to the oversampling of the inner k -space region. After this initial data acquisition, the algorithm proceeds to reacquire data that were obtained during significant coronary distortion, as determined from the inner-spiral images.

Before continuing with a description of the data acquisition strategy, a method must be introduced for evaluating the degree of distortion within each inner-spiral image. This method is the correlation coefficient (CC) template matching algorithm (12,13). In this algorithm, the similarity between an inner-spiral image $f(x, y)$ and the template $h(x, y)$ is evaluated by defining a distance metric:

$$d^2(\xi, \eta) = \sum_{i=1}^M \sum_{j=1}^N \{f'_{(\xi, \eta)}(x_i, y_j) - h'(x_i, y_j)\}^2 \quad [3]$$

$$= 2 - 2 \sum_{i=1}^M \sum_{j=1}^N [f_{(\xi, \eta)}(x_i, y_j) - \bar{f}_{(\xi, \eta)}] \quad [4]$$

$$\times [h(x_i, y_j) - \bar{h}] / (\sigma_{f_{(\xi, \eta)}} \sigma_h M \times N)$$

where:

$$f'_{(\xi, \eta)}(x, y) = [f_{(\xi, \eta)}(x, y) - \bar{f}_{(\xi, \eta)}] / (\sigma_{f_{(\xi, \eta)}} \sqrt{M \times N}) \quad \text{and}$$

$$h'(x, y) = [h(x, y) - \bar{h}] / (\sigma_h \sqrt{M \times N}).$$

$f_{(\xi, \eta)}(x, y)$ is the $M \times N$ pixel region in the image centered at (ξ, η) ; $\bar{f}_{(\xi, \eta)}$ and $\sigma_{f_{(\xi, \eta)}}$ are the mean and standard deviation (SD) of $f_{(\xi, \eta)}(x, y)$; and \bar{h} and σ_h are the mean and SD

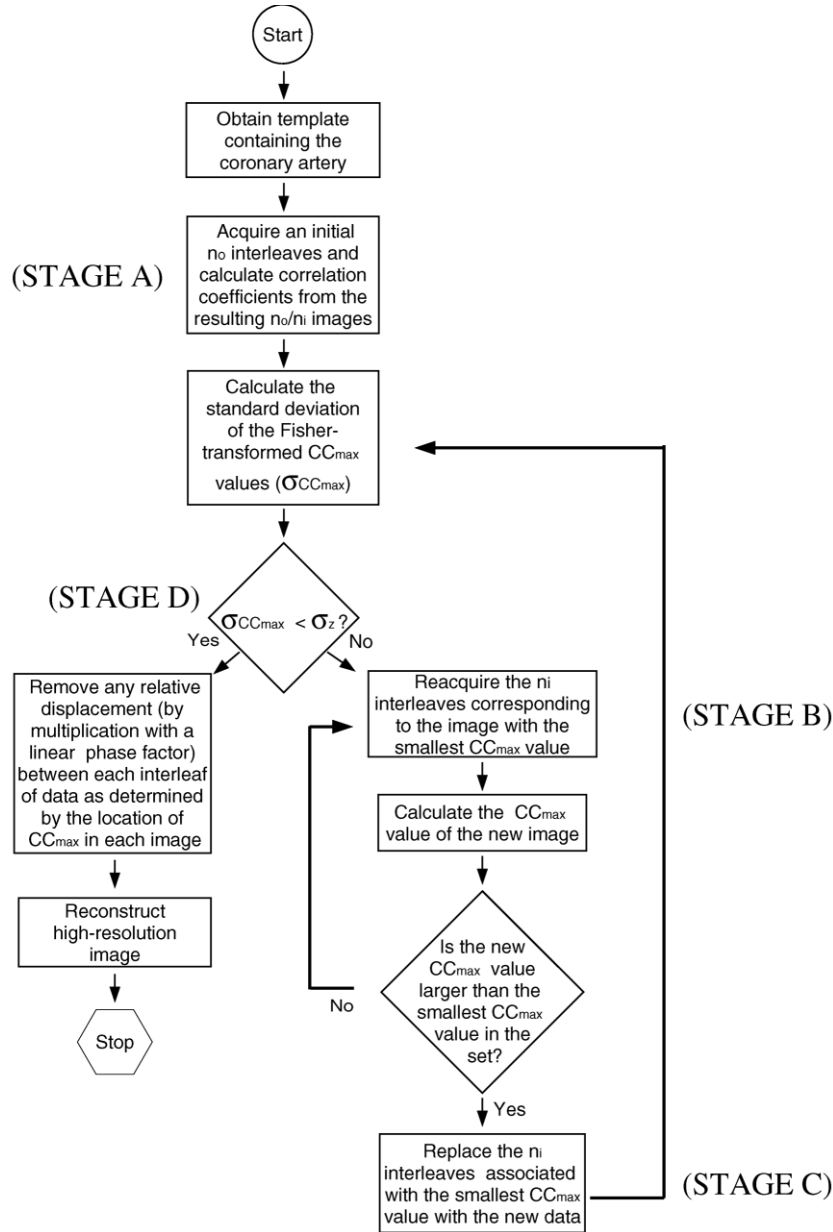


FIG. 3. Flow chart for the VD adaptive imaging technique.

of $h(x, y)$. This particular distance metric is insensitive to any bias and/or gain in the image relative to the template (i.e., $f(x, y)$ and $uf(x, y) + v$; $u, v = \text{constants}$, both have the same $d^2(\xi, \eta)$ values). This property is useful for coronary artery imaging since the presence of flowing blood and/or contrast agent may alter the signal intensity over time. The second term in Eq. [4] can be recognized as the CC between $f_{(\xi, \eta)}$ and h (14). The value of the CC therefore gives an indication of the similarity between the template and image at each location (ξ, η) (Fig. 2b), up to a maximum of one for identity. The location with the largest CC value ($\equiv CC_{max}$) bears the greatest similarity to the template (Fig. 2c).

Continuing on with the data acquisition process, the CC algorithm is applied to the template and each of the n_o/n_i images. The one with the smallest CC_{max} value possesses

the greatest distortion (i.e., the least similarity) relative to the template. The n_i interleaves that were used to form this inner-spiral image (and the associated n_i outer interleaves) are then reacquired (stage B in Fig. 3). The CC algorithm is then applied to the inner-spiral image formed from the n_i newly acquired interleaves. If the new CC_{max} value is larger than the old CC_{max} value, its n_i interleaves replace the old data (stage C in Fig. 3). The algorithm iterates so that the n_i interleaves corresponding to the most distorted data are continually being reacquired. Note that since n_i is small, the entire process of data acquisition, CC_{max} calculation, and interleaf selection is performed in real time.

Using the above algorithm, the relative similarity of the data increases monotonically with time. This process should continue until all n_o/n_i inner-spiral images are identical except for noise. To identify the point at which

this occurs, the expected behavior of CC_{max} in the presence of white, Gaussian noise must be examined. Using the Fisher transform (13,15) ($z = \tanh^{-1}\{CC_{max}\}$), the probability density function of CC_{max} values associated with a template consisting of $M \times N$ pixels applied to an ensemble of identical images can be approximated by a Gaussian distribution, with mean and SD given, respectively, by:

$$\mu_z \approx \tanh^{-1}\{CC_{max}\} \quad [5]$$

$$\sigma_z \approx 0.7 / \sqrt{N \times M - 3} \quad [6]$$

where

$$\langle CC_{max} \rangle = \sigma_h^2 / (\sigma_h^2 + \sigma_n^2),$$

σ_n = SD of the noise distribution.

To evaluate the progress of data acquisition, the SD of the Fisher-transformed CC_{max} values ($\equiv \sigma_{CC_{max}}$) is calculated (stage D in Fig. 3). If systemic differences exist between the images, the expected $\sigma_{CC_{max}}$ value will be given by (16):

$$\langle \sigma_{CC_{max}} \rangle = \sqrt{\sigma_z^2 + \sigma_{sys}^2} \quad [7]$$

where σ_{sys} is the SD of the distribution associated with systemic error. Therefore, if

$$\sigma_{CC_{max}} \leq \sigma_z \quad [8]$$

this implies that the inner-spiral images are identical within the limits of noise, and the algorithm terminates (σ_z is used rather than μ_z because its value is independent of the noise magnitude, which is not precisely known (13,17)). In practice, it was found that better results were achieved if a stability criterion was added into the algorithm termination condition. Specifically, data acquisition was terminated only if, in addition to Eq. [8], no further improvement in CC_{max} values was encountered for 5 s. This stability criterion was found to reduce the likelihood of getting caught inside local $\sigma_{CC_{max}}$ minima, as well as to provide a degree of tolerance for the approximations inherent in the Fisher transform (13,15).

The final stage in the algorithm is combining the full VD-spiral data into a high-resolution image. Before doing so, however, any relative displacement as determined by the location of the CC_{max} values in the inner-spiral images is removed by multiplication in k -space with a linear phase factor. Note that since the algorithm ideally identifies images that differ by at most a rigid-body displacement plus noise, a linear correction is sufficient. (For greater accuracy, displacements were calculated on images interpolated up to a resolution greater than the full-spiral image).

An example VD-spiral acquisition is illustrated in Fig. 4. Figure 4a and b plot the mean and SD of the CC_{max} values of the data as a function of time. As the scan progresses, the increasing CC_{max} values indicate that the relative similarity of the inner-spiral images increases. Full VD-spiral images reconstructed at increasing scan times (Fig. 4e–g)

correspondingly demonstrate a progressive improvement in quality.

METHODS

The objective of the experiments was to evaluate the coronary imaging capabilities of the VD adaptive imaging technique. All experiments were performed on a 1.5T GE SIGNA CV/i scanner (gradient amplitude = 40 mT/m, slew rate = 150 T/m/s) with a BiT3 interface to a Sun Ultra 60 (360 MHz). The associated acquisition and control software was an adapted version of the Stanford real-time system (18).

To explore the effects of inner-spiral spatial and temporal resolution on the motion compensation capabilities of the VD technique, high-resolution coronary artery images were acquired using a range of VD-spiral types (Table 1) conforming to the constraints specified in the Theory section. Each spiral was preceded by a 7-ms spectral-spatial pulse (18) with 5-mm slice thickness. To conform to gradient duty cycle limits, a TR of 40 ms was used. While the temporal resolutions in Table 1 indicate the time for complete inner-spiral image updates, a sliding window reconstruction (18,19) provided partial updates every TR. Due to the short TR, a low flip angle of 30° was necessary to provide an adequate SNR.

Inner-spiral images were reconstructed at a matrix size of 128×128 pixels, with zero padding where necessary. Templates, consisting of 16×16 pixel regions containing the coronary artery, were extracted (based on visual inspection) from initial inner-spiral movie loops. A 16×16 template size was chosen because it was large enough to encompass all coronary artery segments encountered in the experiments. Note, however, that while the total template area is constant for all VD-spiral types, not all pixels are independent at the lower inner-spiral spatial resolutions due to interpolation. Also note that a limitation with a visual template selection is that artifact may be present. To increase the likelihood of obtaining an artifact-free template, three templates from the same cardiac phase, but different cardiac cycles, were selected (again visually) and tracked simultaneously. After template selection, motion compensation was performed prospectively based on CC template matching. Algorithmic decisions were governed by the template with the smallest $\sigma_{CC_{max}}$ value. Image reconstruction and CC algorithm processing required less than 40 ms, and could therefore be performed in real time. For analysis, cardiac plethysmograph and respiratory bellows waveforms were monitored, but were not used to guide the acquisition or correct the images (e.g., Fig. 4c and d).

To determine which VD-spiral type produced the best results, a blinded review of all images was performed by physicists with experience in coronary artery imaging (J.A.S., N.R., and G.A.W.), and a cardiac radiologist (N.M.). In this review, the template regions of each (randomly-ordered) triplet of images produced by the different VD-spiral types were displayed. Reviewers were instructed to rank each image triplet from best to worst based on resolution and vessel conspicuity, but to overlook differences in SNR.

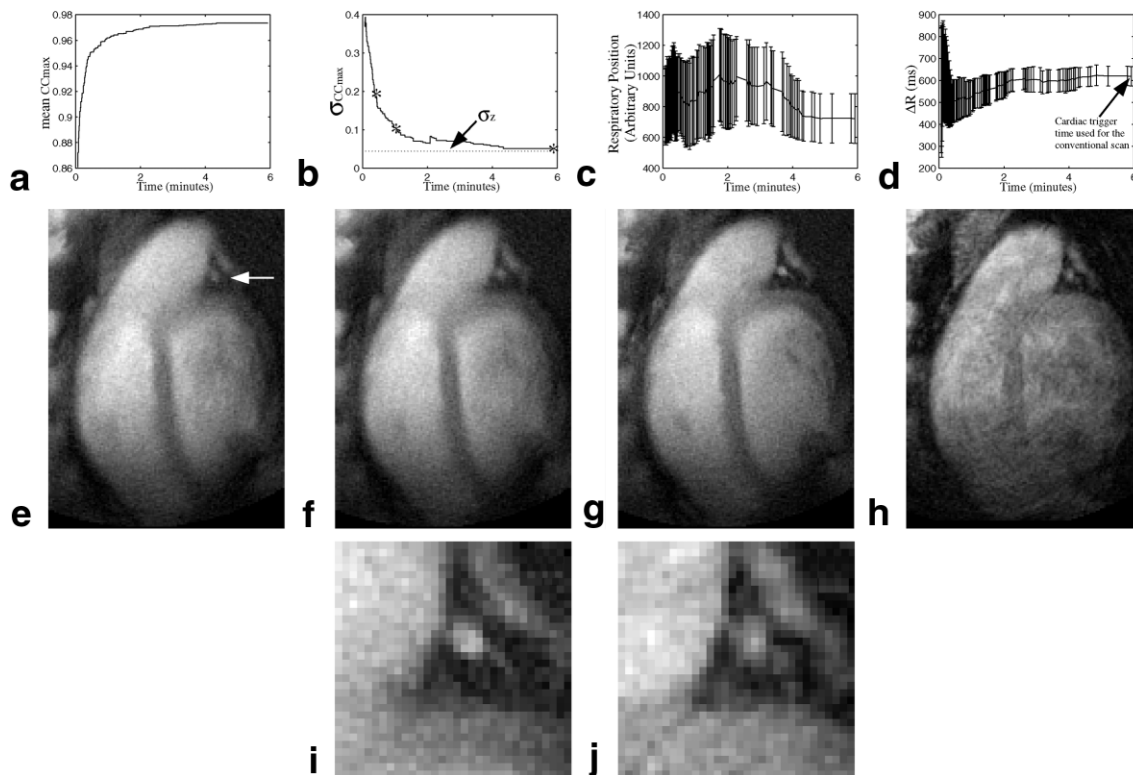


FIG. 4. A VD-spiral acquisition of a cross-sectional view of the left coronary artery. (a) Mean and (b) SD of the CC_{max} values as a function of time. In b, CC_{max} values have been Fisher-transformed to better illustrate the approach to σ_z . c: Respiratory position of the VD-spiral data, as measured by bellows. d: Time between the occurrence of the peak plethysmograph value and the acquisition of the VD spiral interleaves ($=\Delta R$). For c and d, plotted values are the mean \pm SD over the data associated with the VD-spiral interleaves. Full-spiral images reconstructed at (e) $\sigma_{CC_{max}}/\sigma_z = 4.2$, (f) $\sigma_{CC_{max}}/\sigma_z = 2.24$, and (g) $\sigma_{CC_{max}}/\sigma_z = 1.13$. The time points corresponding to images e–g are indicated by the *'s in plot b. h: Cardiac-triggered breath-hold scan at the same location and cardiac phase. The mean final ΔR value in d was used to prescribe the cardiac-trigger time. The coronary artery is indicated by the arrow in e. i and j: Zoomed-in view of template region in g and h, respectively.

The overall motion compensation performance of the VD technique was evaluated by comparing results in the template region with cardiac-triggered breath-hold coronary artery images acquired at the same nominal resolution (0.78 mm). The breath-hold acquisitions used 14-interleaf uniform-density spirals (readout time = 16 ms). One interleaf, but seven 5-mm slices were acquired per heartbeat. Due to the long TR (≈ 1 s), a large flip angle of 90° and 1 NEX provided adequate signal-to-noise ratio (SNR). Respiratory compensation was accomplished with breath-holding, and cardiac-triggering was accomplished using plethysmograph waveforms. Slice lo-

cation was prescribed directly from the VD scan. The cardiac-trigger time was specified from the mean value of the plethysmograph-derived acquisition times of the final data set in each of the $n_i = 4$, $n_o = 20$ VD-spiral acquisitions (see Fig. 4d).

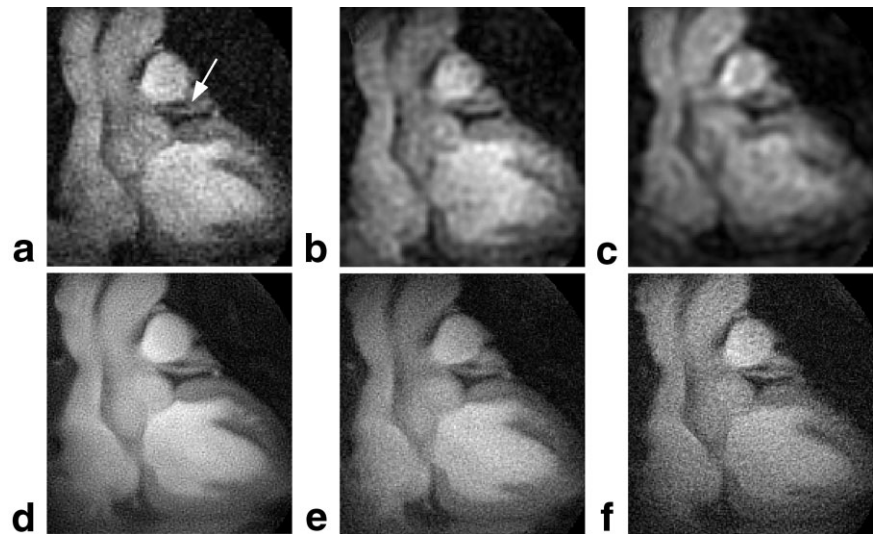
Using the above methods, VD-spiral and conventionally acquired images could be acquired from the same location and cardiac phase. To compare these images, a second blinded evaluation was performed. In this evaluation, the template regions of the VD-spiral and cardiac-triggered breath-hold images were presented (in random order) to each reviewer. For each image pair, the VD-spiral image

Table 1
Parameters Used for the Data Acquisitions

Spiral type	n_i , n_o	Δx_i , Δx_o (mm)	Δt (ms)	NEX	Inner-spiral fraction
VD	6, 30	1.56, 0.78	240	4	0.84
VD	4, 20	2.91, 0.78	160	4	0.66
VD	2, 28	3.66, 0.78	80	2	0.80
Uniform	14	0.78	–	1	–

The first three rows list the parameters for the VD spirals. The last row lists the parameters for the uniform-density spiral used for the cardiac-triggered breath-hold scan. Δx_i , Δx_o are the inner- and full-spiral spatial resolutions respectively. The listed temporal resolution (Δt) is the time required for a full inner-spiral image update with a TR of 40 ms. The last column is the fraction of readout time occupied by the inner spiral.

FIG. 5. Comparison of left coronary artery images resulting from the different VD-spiral types. Inner-spiral images from (a) $n_i = 6$ (1.56-mm resolution), (b) $n_i = 4$ (2.91-mm resolution), and (c) $n_i = 2$ (3.66-mm resolution) VD acquisitions. Corresponding full-spiral images (all 0.78-mm resolution) with (d) $n_o = 30$, 4 NEX, (e) $n_o = 20$, 4 NEX, (f) $n_o = 28$, 2 NEX. The coronary artery is indicated by the arrow in a. The SNR in the coronary artery is 8.2, 7.3, and 5.8 in images d, e, and f, respectively.



presented was the one selected as the best from the three different VD-spiral types in the earlier blinded triplet evaluation. A score was assigned according to the image on the left being significantly poorer, poorer, equivalent, better, or significantly better than the image on the right. Reviewers were instructed to base their evaluations on image resolution and vessel conspicuity, but to overlook differences in SNR and contrast. For further evaluation, coronary vessel diameter, SNR, contrast-to-noise ratio (CNR), and visible vessel length were also compared between each image pair.

A total of nine coronary artery segments in seven healthy volunteers were imaged using a variety of slice orientations. On three subjects, only an $n_i = 4$, $n_o = 20$ VD-spiral image was acquired. All experiments were conducted in compliance with institutional ethics guidelines for human studies.

RESULTS

A comparison of the results of imaging with the three VD-spiral types used in this study is given in Fig. 5. The different inner-spiral spatial resolutions of each of the VD spirals can be observed in Fig. 5a–c. To provide a fair comparison, all

inner-spiral images were interpolated to the same number of pixels as the full-spiral images, displayed in Fig. 5d–f. The resolution in the full-spiral images is substantially improved relative to the inner-spiral ones. Furthermore, despite the fact that data acquisition occurs over multiple cardiac and respiratory cycles, the full-spiral images have no obvious artifacts relative to the “instantaneously” acquired inner-spiral images. This provides the first evidence that the VD algorithm is successful in compensating for the effects of coronary motion. Due to the variability in total data acquisition time (in accordance with design constraint #4), the full-spiral images possess different SNRs (listed in the figure). These vary roughly as the square root of Eq. [2], as expected. In terms of vessel sharpness, all full-spiral images appear to be similar. However, Fig. 5f actually represents one of the better $n_i = 2$, $n_o = 28$ images. A more representative result is Fig. 6. In this case, the coronary in the $n_i = 2$, $n_o = 28$ image appears to be significantly less sharp than in the other full-spiral images. Between the two higher inner-spiral spatial resolution images, motion compensation performance appears to be roughly equivalent (although the $n_i = 6$, $n_o = 30$ acquisition may be slightly better). Table 2 lists the data from the blinded evaluation of the template regions of images corresponding to the three VD-spiral types. In accordance with the above

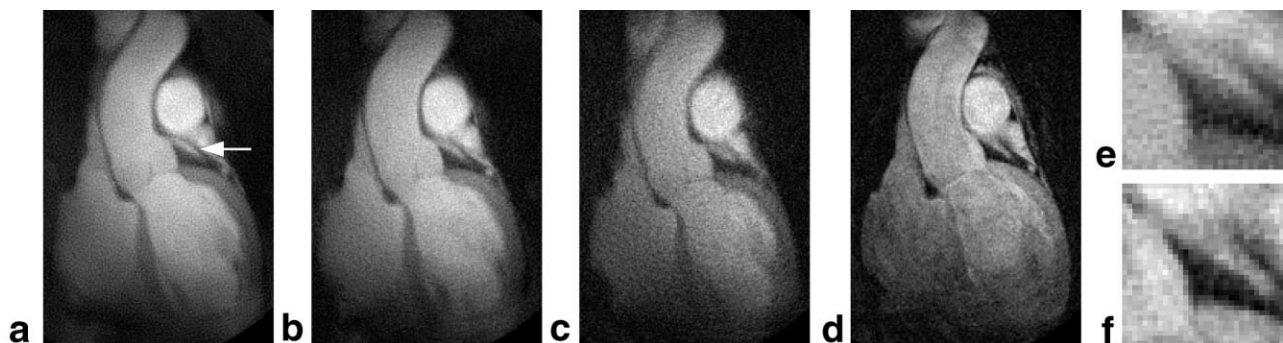


FIG. 6. Comparison of left coronary artery images produced from the different VD-spiral types. Full-spiral images corresponding to VD acquisitions with (a) $n_i = 6$, $n_o = 30$ (b) $n_i = 4$, $n_o = 20$, and (c) $n_i = 2$, $n_o = 28$. d: Cardiac-triggered breath-hold scan at the same location and cardiac phase. The coronary artery is indicated by the arrow in a. e and f: Zoomed-in view of template region in a and d, respectively.

Table 2
Results for the Evaluation of the Template Regions of Images
Corresponding to the Three Different VD-Spiral Types

Ranking \ n_i, n_o	6, 30	4, 20	2, 28
Best	70.8%	29.2%	0%
Intermediate	12.5%	62.5%	25%
Worst	16.7%	8.3%	75%

Entries represent the percentage of images that were ranked as having the best, intermediate, and worst quality among each triplet of VD spiral images. A total of six image triplets were evaluated by four blinded reviewers.

observations, the data indicate that image quality increases with improving inner-spiral spatial resolution. However, the improvement at the two highest inner-spiral spatial resolutions is less substantial than at the lowest.

Further support for the observed effects of inner-spiral spatial and temporal resolution is supplied by an examination of the elapsed time between the VD spiral interleaves and the peak value of the plethysmograph waveform ($=\Delta R$). A typical example is plotted in Fig. 4d. As the scan progresses, the distribution of ΔR values among the VD-spiral interleaves converges. The distribution of ΔR values among the final set of VD spiral interleaves provides an indication of the technique's ability to identify data from the correct phase of the cardiac cycle. The sixth column in Table 4 lists the SD of the ΔR values ($=\sigma_{\Delta R}$) for the different VD-spiral types. The $n_i = 4$, $n_o = 20$ and the $n_i = 6$, $n_o = 30$ values are similar, but the $\sigma_{\Delta R}$ value of the $n_i = 2$, $n_o = 28$ VD spiral is significantly larger. This implies that the $n_i = 2$, $n_o = 28$ type is poorer at identifying data from the correct phase of the cardiac cycle, which supports the previous observations.

The results of the blinded comparison between the VD-spiral and cardiac-triggered breath-hold images in the template region are listed in Table 3. The data indicate that the VD-spiral technique provides images of equal or better quality in the template region in roughly half the cases. This implies that local motion compensation performance is roughly equivalent between the two techniques. An example comparison is illustrated in Fig. 7. In the template region around the right coronary artery (a zoomed-in view is illustrated in Fig. 7e and f), the majority of the reviewers scored the template regions of the images as being of equivalent quality. Note, however, that in regions remote from the coronary artery (e.g., the ventricular wall border), some edge blurring is observed in the VD-spiral image. This is likely due to the fact that, since cardiac motion is non-rigid body (2), motion compensation was not necessarily optimal for locations outside the template region. As another example, Fig.

4g and h (zoomed-in view in Fig. 4i and j) illustrate a case in which reviewers scored the VD-spiral images as having better quality at the template location. Figure 6 illustrates an example in which the VD-spiral image (Fig. 6a) was rated as having an inferior quality to the cardiac-triggered breath-hold scan at the template region (Fig. 6e and f).

The results of the quantitative comparison between the VD-spiral and cardiac-triggered breath-hold images are listed in Table 4. The second column compares the difference in measured coronary vessel diameters ($=\Delta D$). (Only the $n_i = 4$, $n_o = 20$ images were used for comparison, because these were the acquisitions that were used to directly prescribe the cardiac-triggered breath-hold scans). Since the maximum ΔD is less than half a pixel, there is no significant difference between these two types of scans. The fifth column lists the difference in visible vessel length in the two types of images. The results indicate only a slight difference between the two types of scans, likely accounted for by small differences in slice location or position within the cardiac cycle. The overall visible vessel length varied between 19 and 33 mm, which is short in comparison with recent reports (20). This is because imaging was restricted to 2D, and scan planes were not optimized for maximal vessel visibility.

In comparing the SNR between the VD-spiral and cardiac-triggered breath-hold images, one must consider that all VD-spiral scans had longer data acquisition times (≥ 20 interleaves and ≥ 2 NEX vs. 14 interleaves and 1 NEX for the cardiac-triggered breath-hold scans). When these factors are taken into account, the third column in Table 4 indicates that the SNR efficiency ($= \text{SNR} / \sqrt{\text{data acquisition time}}$) of the VD images is about half that of the cardiac-triggered breath-hold scans. This discrepancy is likely due to differences in flip angle, since the theoretical ratio of 0.5 ($= \sin(30^\circ)/\sin(90^\circ)$) is close to the experimentally observed value. This implies that inflow effects are likely the dominant factor in determining SNR in both cases. Similar results are also obtained when the CNR of the two scans is compared (fourth column of Table 4).

DISCUSSION

Effect of Inner-Spiral Spatial/Temporal Resolution on Motion Compensation Performance

The performance of the VD technique is dependent on the inner-spiral spatial and temporal resolution. In this study, it was found that effects of spatial resolution dominate. In the section below, these results are interpreted.

Effects of Inner-Spiral Spatial Resolution

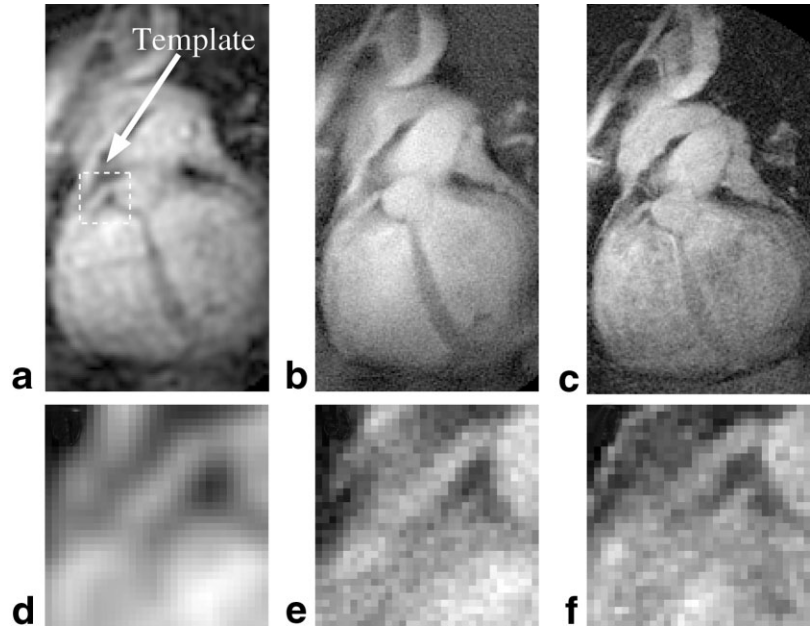
At first, one might expect that it would be difficult to correct for the effects of motion in a high-resolution image

Table 3
Results for the Comparison of the Template Regions of VD-Spiral and Cardiac-Triggered Breath-Hold Images

Image quality	Significantly poorer	Poorer	Equivalent	Better	Significantly better
% of images	8.3%	33.3%	22.2%	27.8%	8.3%

Entries represent the percentage of time that the VD spiral images were ranked as significantly poorer, poorer, equivalent, better, and significantly better than the corresponding cardiac-triggered breath-hold scans. A total of nine image pairs were evaluated by four blinded reviewers.

FIG. 7. Comparison of VD-spiral and cardiac-triggered breath-hold acquisitions of the right coronary artery. (a) Inner- (2.91-mm resolution) and (b) full- (0.78-mm resolution) spiral images acquired with the $n_i = 4$, $n_o = 20$ VD spiral. The location of the template containing the coronary artery that was used for this acquisition is indicated by the dashed rectangle in a. c: Cardiac-triggered breath-hold spiral image (14 interleaves, 0.78-mm resolution) at the same location and cardiac phase. d-f: Zoomed-in view of template region in a-c, respectively.



based on motion-tracking information acquired at a much lower spatial resolution. However, as pointed out by Hajnal et al. (21), a distinction must be made between image resolution and the ability to detect displacement. In MR images, which are strictly band-limited by the nature of the k -space acquisition, relative displacement can be determined to an arbitrary degree of precision through interpolation, regardless of the initial resolution. In practice, such precision will be possible only if all images are identical (in the ROI) except for rigid-body translations. The objective of the CC technique is to identify a set of such images. Its ability to do so, however, is limited by the presence of noise. A description of the noise sensitivity of the CC technique is given (via Eqs. [5] and [6]) by the CC_{max} SNR:

$$SNR_{CC_{max}} \equiv \mu_z / \sigma_z = \tanh^{-1} \{ \sigma_h^2 / (\sigma_h^2 + \sigma_n^2) \} / (0.7 / \sqrt{M \cdot N - 3}). \quad [9]$$

Consider an original template with resolution δ_o , noise σ_{n_0} , pixel SD σ_{h_0} , and size $M \times N$. As the resolution (δ) improves, $SNR_{CC_{max}}$ can be rewritten as a function of δ :

$$SNR_{CC_{max}} = 1.43 \tanh^{-1} \{ \sigma_{h_0}^2 / (\sigma_{h_0}^2 + [\sigma_{n_0} \delta_o / \delta]^2) \} \sqrt{M \times N \cdot (\delta_o / \delta)^2 - 3} \quad [10]$$

assuming that:

$$\sigma_n \propto 1 / [(\text{pixel area}) \sqrt{\text{data acquisition time}}].$$

A plot of Eq. [10] using typical values from the experiments is displayed in Fig. 8. If the inner-spiral resolution is too low, the technique's ability to identify appropriate data may be limited by low $SNR_{CC_{max}}$. As the resolution improves, $SNR_{CC_{max}}$ increases. This may explain why full-spiral image quality was found to increase with improving inner-spiral spatial resolution. Note, however, that a point is reached where the benefits of increased number of pixels in the tem-

Table 4
Quantitative Results of the VD-Spiral Experiments

n_i, n_o	ΔD (pixels)	SNR_{VD}/SNR_{CTBH}	CNR_{VD}/CNR_{CTBH}	Length (mm)	$\sigma_{\Delta R}$ (msec)	Δy (pixels)
6, 30	—	0.55 ± 0.08	0.38 ± 0.08	—	51 ± 22	2.5 ± 0.6
4, 20	0.41 ± 0.1	0.59 ± 0.1	0.42 ± 0.12	-1.2 ± 5.7	59 ± 28	2.4 ± 0.8
2, 28	—	0.47 ± 0.05	0.41 ± 0.06	—	139 ± 100	2.2 ± 1.1

The second column is the maximum difference in coronary artery diameter (ΔD) between each pair of VD-spiral and cardiac-triggered breath-hold images. The third and fourth columns list the ratio of the SNR, and CNR per square root data acquisition time between the VD-spiral and cardiac-triggered breath-hold images at the coronary artery. The CNR was calculated as the difference between the mean of the ten largest pixel intensities in the coronary artery, and the mean of the ten lowest pixel intensities in the template. The fifth column lists the difference in vessel length visible between the VD-spiral and cardiac-triggered breath-hold scans. The sixth column lists the standard deviation of the ΔR values in the final images for each of the VD-spiral types. The last column is the relative pixel displacement (Δy) in the final VD data sets (before it is removed). All entries are listed as the mean \pm standard deviation calculated over the nine coronary artery segments evaluated in this study. In two images, however, vessel length and diameter comparisons could not be performed due to inadequate image quality and inappropriate vessel orientation.

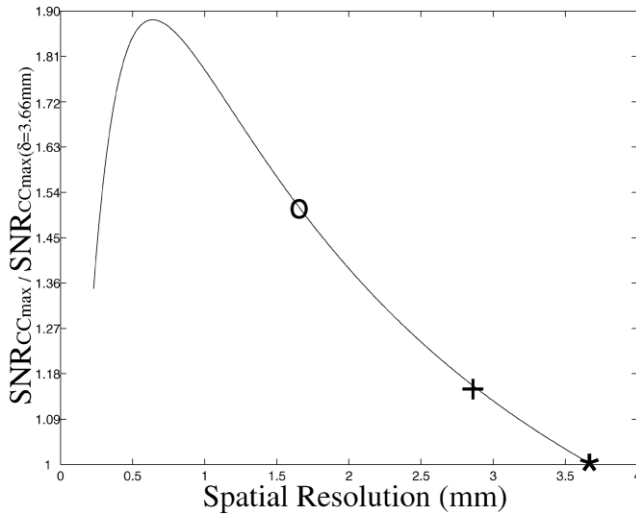


FIG. 8. Plot of SNR_{CCmax} (normalized to the value at $\delta = 3.66$ mm) vs. resolution. The parameters used to calculate the curve, $\sigma_{h_0}/\sigma_{n_0} = 7$, $M \times N = 256$, and $\delta_0 = 3.66$ mm were typical values from the experiments. The symbols indicate the theoretical SNR_{CCmax} values of the $n_i = 2$, $n_o = 28$ (*), $n_i = 4$, $n_o = 20$ (+), and $n_i = 6$, $n_o = 30$ (○) VD spirals, respectively.

plate loses out to the increased noise associated with better resolution. This places a limit on the improvement in performance that can be expected through increased inner-spiral spatial resolution.

Effects of Inner-Spiral Temporal Resolution

In the present study, the temporal resolution ranged from 80 ms to 240 ms (see Table 1). By way of comparison, conventional scans typically employ a temporal window of at most 150 ms, and frequently less than 30 ms (22,23). Data acquired over an extended period of time may experience temporal blurring (24–26). This blurring reduces the effective resolution of the inner-spiral images and, via Eq. [10], reduces the sensitivity of the CC algorithm's ability to identify acceptable data. In this study, it was found that the inner-spiral temporal resolution did not play as strong a role as inner-spiral spatial resolution in determining motion compensation performance. In part, this may be due to the fact that partial image updates were provided at higher temporal resolutions using a sliding window reconstruction. An additional consideration is that template selection may have been biased toward points in the cardiac cycle with minimal motion, since these periods would have corresponded to the best inner-spiral images. On the other hand, temporal resolution limitations may have been the reason why only minimal improvement in motion compensation performance of the $n_i = 6$, $n_o = 30$ over the $n_i = 4$, $n_o = 20$ was observed—despite the substantial improvement in inner-spiral spatial resolution and SNR_{CCmax} (Table 1 and Fig. 8).

Comparison of the VD-Spiral Technique With Conventional Methods

Breath-Holding

The results of this study indicate that image quality was roughly comparable within the template regions of the

VD-spiral and cardiac-triggered breath-hold images. Since these two very different approaches provide equivalent image quality, this suggests that, at the current resolution (0.78 mm), both techniques are proficient at suppressing the effects of coronary motion in healthy subjects. This provides a strong motivation for the exploration of higher resolutions with the VD-spiral technique.

An advantage of the VD-spiral technique is that, since direct coronary visualization is used for compensation, it is not expected to be adversely affected in subjects with arrhythmias, for whom cardiac-triggering is difficult and/or breath-holding is not possible. While such constraints were not an issue in the healthy population examined in this study, they are much more likely to occur in elderly patients with coronary disease (8). Furthermore, the longer scan times and greater SNR requirements associated with even higher-resolution acquisitions may actually preclude the use of breath-holding entirely. On the other hand, the greater SNR efficiency and multislice capability of the cardiac-triggered breath-hold method provide it with advantages over the VD-spiral technique.

Navigator Echoes

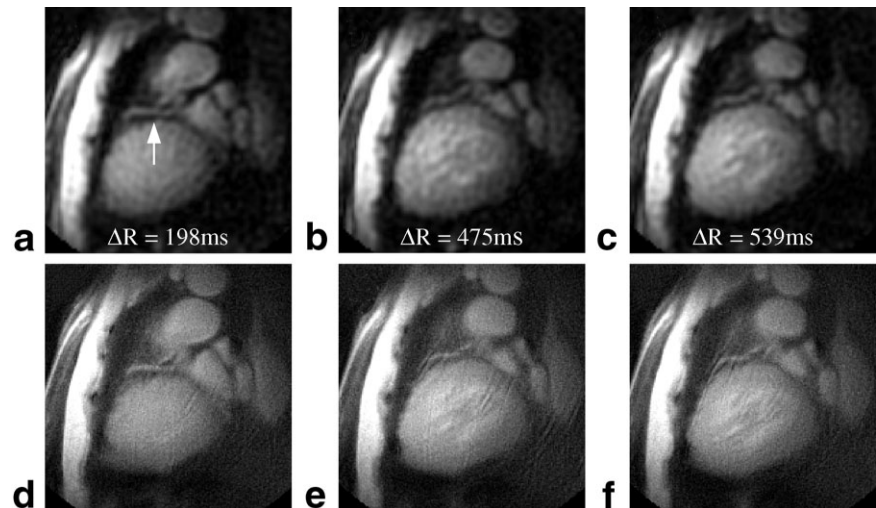
The other major approach currently used for motion compensation is navigator echoes. Like the VD-spiral technique, navigator echoes are potentially more applicable to the patient population than breath-holding (8). Navigator-echo methods rely on cardiac-triggering, however, and are thus still sensitive to arrhythmias.

The VD-spiral technique may provide improved efficiency over navigator methods due to the nature of the data acquired. If one examines Fig. 4c, a typical experimental result, the distribution of the bellows-derived respiratory positions as a function of scan time does not appear to exhibit a particularly strong convergence. This implies that the VD-spiral technique is tolerant of a large range of respiratory phases. To further elucidate the nature of the data, one can examine the displacement in the final VD data set. The last column of Table 4 indicates displacements up to 8 mm. While the displacement tolerance of some navigator techniques lie within this range (27), this relates specifically to diaphragm position. A number of studies have demonstrated that actual coronary displacement may be less than half this value (1,7). In contrast, values listed in Table 4 refer to actual coronary displacement. On the other hand, recent studies using slice-following techniques demonstrated significantly improved navigator-echo efficiencies ($\geq 70\%$) (28). Further study is therefore required to elucidate the exact nature of the data selected by the two approaches.

Limitations and Future Directions

The results of this study demonstrated that the VD-spiral technique possesses a number of advantages relative to conventional methods. However, there are also a number of drawbacks. The first drawback is the poor SNR efficiency associated with the short TR and flip angle of the technique (about half that of conventional approaches). As noted earlier, the signal strength in both cases appears to be dominated by inflow effects. This implies that, in ret-

FIG. 9. Three of five frames from a high-resolution VD-spiral movie acquired using templates from different phases of the heart cycle. **a–c**: Inner- and **d–f** corresponding full-spiral images ($n_i = 4$, $n_o = 20$). The phase of the cardiac cycle is indicated by the ΔR value. The coronary artery is indicated by the arrow in **a**.



respect, the empirically-selected 30° flip angle for VD-spirals was likely too small, and should be increased in the future. Another possible method to improve SNR is the use of intravascular contrast agents (29).

A second limitation is that because the CC algorithm is targeted at the template region specifically, motion compensation may be degraded in remote areas. While larger templates could be used to overcome this problem, reduced scan efficiency may result, as the probability of rigid-body motion occurring over the larger area would be reduced. An alternative strategy could be to use a grid of small templates covering a larger total area (30). In this case, a large area could be covered, but efficiency may not suffer because each grid element could be tracked independently.

The ultimate motion compensation performance of the VD-spiral technique is limited by the inner-spiral spatial and temporal resolution. In the future, strategies that provide added flexibility to the VD-spiral design may result in further performance improvements. One possible approach is to utilize partial k -space acquisitions. A recent study has demonstrated the extension of real-time imaging into the submillimeter domain using this approach (29). Another strategy is to employ one of the recently developed parallel imaging strategies (e.g., sensitivity encoding (SENSE) (31,32) or simultaneous acquisition of spatial harmonics (SMASH) (33)). This would provide added flexibility in trading off the inner-spiral spatial and temporal resolution, over and above that achieved with the native VD-spiral design. Another possible means of expanding the range of spatial/temporal resolution could be the use of non-spiral VD trajectories such as VD-echo-planar imaging (EPI) (34) or projection reconstruction (35). Schaffter et al. (36) have already demonstrated a form of direct motion compensation by employing the latter approach. Pipe (37) has also developed a direct motion compensation method employing a related VD strategy.

Another limitation of the VD-spiral technique is that it is currently restricted to 2D imaging. If 3D adaptive imaging could be achieved, a greater extent of the tortuous coronary tree could be visualized, and SNR may be improved. To implement 3D adaptive imaging, one could perform a

full 3D VD-spiral acquisition. The problem with this approach is that a real-time implementation is unlikely. Another possibility is to use multiband encoding. In this case, the major challenge is to ensure that the inner-spiral image appearance is consistent for all basis function acquisitions. Presently, some early work on this approach has been undertaken using a complex Hadamard basis set (38).

A final limitation of the present implementation of the VD-spiral technique is that data from only one point in the cardiac cycle are acquired. In the future, the technique could be extended to an arbitrary number of cardiac phases by tracking multiple templates simultaneously from different phases of the cardiac cycle. An initial experiment was performed to demonstrate the feasibility of such an approach using five templates from different cardiac phases. The results are displayed in Fig. 9. The different phases of the heart cycle can be inferred by noting the changing orientation of the coronary anatomy from one image to the next.

CONCLUSIONS

The results of this study indicate that the VD adaptive imaging technique is capable of generating submillimeter coronary artery images. Motion compensation for these scans was performed prospectively, with information provided directly from the coronary anatomy. Motion compensation performance was found to be affected by the inner-spiral spatial and temporal resolution, with inner-spiral spatial resolution being the primary determinant of final image quality. At the highest inner-spiral spatial resolutions, however, poor temporal resolution may have limited the performance of the technique.

A drawback of the VD spiral technique is that, due to the short TR and low flip angle, SNR is reduced relative to conventional scans. This limited the efficiency of the algorithm, as multiple averages were required to achieve adequate SNR. However, unlike conventional methods, the VD-spiral technique did not require cardiac-triggering, breath-holding, or navigator echoes. Consequently, its performance is not expected to be affected in patients in whom arrhythmias may be present, and/or for whom

breath-holding may not be possible. In the current study of healthy subjects, results indicated that image quality in the template region was roughly equivalent to conventionally acquired cardiac-triggered, breath-hold acquisitions at the 0.78-mm resolution examined. A number of proposals have been put forth that have the potential to improve the performance of the technique. The VD-spiral adaptive imaging technique may thus prove valuable in expanding the capability and applicability of MR coronary artery imaging.

ACKNOWLEDGMENTS

The authors thank John Pauly for advice on the VD-spiral design, and Mark Henkelman for helpful discussions. The work contained within this paper was supported by the Heart and Stroke Foundation of Canada and the Canadian Institutes of Health Research.

REFERENCES

- Wang Y, Riederer SJ, Ehman RL. Respiratory motion of the heart: kinematics and the implications for the spatial resolution in coronary imaging. *Magn Reson Med* 1995;33:713–719.
- Wang Y, Vidan E, Bergman GS. Cardiac motion of coronary arteries: variability in the rest period and implications for coronary MR angiography. *Radiology* 1999;213:751–758.
- Sussman MS, Kerr AB, Pauly JM, Merchant N, Wright GA. Tracking the motion of the coronary arteries with the correlation coefficient. In: *Proceedings of the 7th Annual Meeting of ISMRM, Philadelphia*, 1999. p 1267.
- Korin H, Felmlee J, Ehman R, Riederer S. Adaptive technique for three-dimensional MR imaging of moving structures. *Radiology* 1990;177:217–221.
- Edelman RR, Manning WJ, Burstein D, Paulin S. Coronary arteries: breath-hold MR angiography. *Radiology* 1991;181:641–643.
- Nehrke K, Bornert P, Manke D, Bock JC. Free-breathing cardiac MR imaging: study of implications of respiratory motion—initial results. *Radiology* 2001;220:810–815.
- Keegan J, Gatehouse P, Yang GZ, Firmin D. Coronary artery motion with the respiratory cycle during breath-holding and free-breathing: implications for slice-followed coronary artery imaging. *Magn Reson Med* 2002;47:476–481.
- Taylor AM, Keegan J, Jhooti P, Gatehouse PD, Firmin DN, Pennell DJ. Differences between normal subjects and patients with coronary artery disease for three different MR coronary angiography respiratory suppression techniques. *J Magn Reson Imaging* 1999;9:786–793.
- Hardy CJ, Saranathan M, Zhu Y, Darrow RD. Coronary angiography by real-time MRI with adaptive averaging. *Magn Reson Med* 2000;44:940–946.
- Spielman DM, Pauly JM, Meyer CH. Magnetic resonance fluoroscopy using spirals with variable sampling densities. *Magn Reson Med* 1995;34:388–394.
- Yudilevich E, Stark H. Spiral sampling in magnetic resonance imaging—the effect of inhomogeneities. *IEEE Trans Med Imaging* 1987;6:337–345.
- Sussman MS, Wright GA. The correlation coefficient technique for pattern matching. In: *Proceedings of the 7th Annual Meeting of ISMRM, Philadelphia*, 1999. p 2003.
- Sussman MS, Wright GA. Factors affecting the correlation coefficient template matching algorithm with application to real-time 2D coronary artery MR imaging. *IEEE Trans Med Imaging* 2002, in press.
- Taylor JR. *An introduction to error analysis*. CA: University Science Books; 1982.
- von Mises R. *Mathematical theory of probability and statistics*. New York: Academic Press; 1964.
- Larsen RJ, Marx MM. *An introduction to mathematical statistics and its applications*. Englewood Cliffs, New Jersey: Prentice Hall; 1986.
- David FN. *Tables of the ordinates and probability integral of the distribution of the correlation coefficient in small samples*. Cambridge: The University Press; 1938.
- Kerr AB, Pauly JM, Hu BS, Li KC, Hardy CJ, Meyer CH, Macovski A, Nishimura DG. Real-time interactive MRI on a conventional scanner. *Magn Reson Med* 1997;38:355–367.
- Riederer SJ, Tasciyan T, Farzaneh F, Lee JN, Wright RC, Herfkens RJ. MR fluoroscopy: technical feasibility. *Magn Reson Med* 1988;8:1–15.
- Slavin GS, Riederer SJ, Ehman RL. Two-dimensional multishot echoplanar coronary MR angiography. *Magn Reson Med* 1998;40:883–889.
- Hajnal JV, Saeed N, Soar EJ, Oatridge A, Young IR, Bydder GM. A registration and interpolation procedure for subvoxel matching of serially acquired MR images. *J Comput Assist Tomogr* 1995;19:289–296.
- Pat GL, Meyer C, Nishimura D. Effects of vessel motion in coronary MRA. In: *Proceedings of the 5th Annual Meeting of SMR, Vancouver*, 1997. p 837.
- Wang Y, Ehman RL. Retrospective adaptive motion correction for navigator-gated 3D coronary MR angiography. *J Magn Reson Imaging* 2000;11:208–214.
- Wood ML, Henkelman RM. MR image artifacts from periodic motion. *Med Phys* 1985;12:143–151.
- Wang Y, Grist TM, Korosec FR, Cristy PS, Alley MT, Polzin JA, Mistretta CA. Respiratory blur in 3D coronary MR imaging. *Magn Reson Med* 1995;33:541–548.
- Hofman MBM, Wickline SA, Lorenz CH. Quantification of in-plane motion of the coronary arteries during the cardiac cycle: implications for acquisition window duration for MR flow quantification. *J Magn Reson Imaging* 1998;8:568–576.
- Danias PG, McConnell MV, Khasgiwala VC, Chuang ML, Edelman RR, Manning WJ. Prospective navigator correction of image position for coronary MR angiography. *Radiology* 1997;203:733–736.
- Saranathan M, Ho VB, Hood MN, Foo TK, Hardy CJ. Adaptive vessel tracking: automated computation of vessel trajectories for improved efficiency in 2D coronary MR angiography. *J Magn Reson Med* 2001;14:368–373.
- Nayak KS, Pauly JM, Yang PC, Hu BS, Meyer CH, Nishimura DG. Real-time interactive coronary MRA. *Magn Reson Med* 2001;46:430–435.
- Sussman MS, Robert N, Wright GA. Artifact-free, maximal-SNR, efficient image combination for coronary MR using the correlation coefficient template grid matching technique. In: *Proceedings of the 9th Annual Meeting of ISMRM, Glasgow, Scotland*, 2001. p 775.
- Pruessmann KP, Weiger M, Scheidegger MB, Boesiger P. SENSE: sensitivity encoding for fast MRI. *Magn Reson Med* 1999;42:952–962.
- Pruessmann KP, Weiger M, Bornert P, Boesiger P. Advances in sensitivity encoding with arbitrary k-space trajectories. *Magn Reson Med* 2001;46:638–651.
- Sodickson DK, Manning WJ. Simultaneous acquisition of spatial harmonics (SMASH): fast imaging with radiofrequency coil arrays. *Magn Reson Med* 1997;38:591–603.
- McKenzie CA, Yeh EN, Ohliger MA, Price MD, Sodickson DK. Self-calibrating parallel imaging with automatic coil sensitivity extraction. *Magn Reson Med* 2002;47:529–538.
- Song HK, Dougherty L, Schnall MD. Simultaneous acquisition of multiple resolution images for dynamic contrast enhancement. *Magn Reson Med* 2001;46:503–509.
- Schaffter T, Rasche V, Carlsen IC. Motion compensated projection reconstruction. *Magn Reson Med* 2001;41:954–963.
- Pipe JG. Motion correction with PROPELLER MRI: application to head motion and free-breathing cardiac imaging. *Magn Reson Med* 1999;42:963–970.
- Cunningham CH, Wright GA, Wood ML. Complex Hadamard encoding for improved temporal information. In: *Proceedings of the 10th Annual Meeting of ISMRM, Honolulu*, 2002. p 298.